CHEMISTRY OF MATERIALS

pubs.acs.org/cm

Article

Breaking the Aristotype: Featurization of Polyhedral Distortions in Perovskite Crystals

Kazuki Morita, Daniel W. Davies, Keith T. Butler,* and Aron Walsh*

Cite This: *Chem. Mater.* 2022, 34, 562−573

Read Online

ACCESS | Metrics & More | Article Recommendations | Supporting Information

ABSTRACT: While traditional crystallographic representations of structure play an important role in materials science, they are unsuitable for efficient machine learning. A range of effective numerical descriptors have been developed for molecular and crystal structures. We are interested in a special case, where distortions emerge relative to an ideal high-symmetry parent structure. We demonstrate that irreducible representations form an efficient basis for the featurization of polyhedral deformations with respect to such an aristotype. Applied to a data set of 552 octahedra in ABO_3 perovskite-type materials, we use unsupervised machine learning with irreducible representation descriptors to identify four distinct classes of behaviors, associated with predominately corner, edge, face, and mixed connectivity between neighboring octahedral units. Through this analysis, we identify $SrCrO_3$ as a material with tunable multiferroic behavior. We further show, through supervised machine learning, that thermally activated structural distortions of $CsPbI_3$ are well described by this approach.

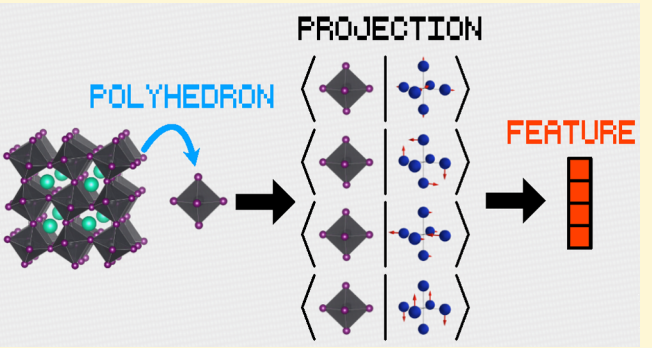

INTRODUCTION

Materials informatics has grown into a substantial field, supported by the surge in the development of machine learning (ML) techniques.[1−4] Although classical ML and deep neural networks have shown success in fields such as image and natural language processing, their efficiency for material structure inputs is still limited. The problem originates from the difficulty in encoding domain knowledge of material science onto ML training. In other words, the crystallographic information stored in materials data sets is not fully used. To improve this, intense efforts have been made to design efficient material representations to featurize the high structural degrees of freedom into a compact size.[2,5−7]

Unless specially tailored ML models are used,[8−10] a number of criteria exist for crystal features. First, a feature must not depend on the permutation of symmetry equivalent atoms, because atomic indices are only defined for convenience and they have little physical meaning.[10] Second, it should not depend on the choice of the unit cell orientation; that is, it should not depend on translation or rotation of the axes. Lastly, it must have a suitable size, with the optimal size depending on the problem of interest. If the target properties are complicated, it will require more dimensions to describe it, whereas if the feature is unnecessarily large, more data will be required to train the ML model due to the "curse of dimensionality".[11] Additionally, physical transparency is favorable since it is becoming possible to relate model predictions with the feature(s) responsible.[12]

Material structures would have been easier to represent if we were able to apply a filter to smear atomistic properties in a mean-field manner. Although such coarse-graining has been studied,[13,14] it is often the case that the local structural properties of a material could induce a non-negligible effect on macroscopic properties. For example, in the perovskite structure type, slight displacement of the B-site cation could induce both a local electric dipole as well as macroscopically observable ferroelectric behavior.[15,16] Another example in a recent study revealed that, for the spin−orbit coupling induced Dresselhaus effect, local inversion symmetry, rather than the global crystal symmetry, is responsible.[17] Other interesting phenomena such as Jahn−Teller distortions, orbital orderings, and magnetic disorders are known, and their coexistence has been reported.[18−20] Given this importance of local structure, many analysis methods have been developed.

There are numerous ways of obtaining a structural feature including Voronoi decomposition, radial distribution functions, nearest neighbors, and electrostatic Ewald summation.[21] Some efforts have been put into the development of calculating

Received: August 27, 2021
Revised: December 17, 2021
Published: January 6, 2022

https://doi.org/10.1021/acs.chemmater.1c02959
Chem. Mater. 2022, 34, 562−573

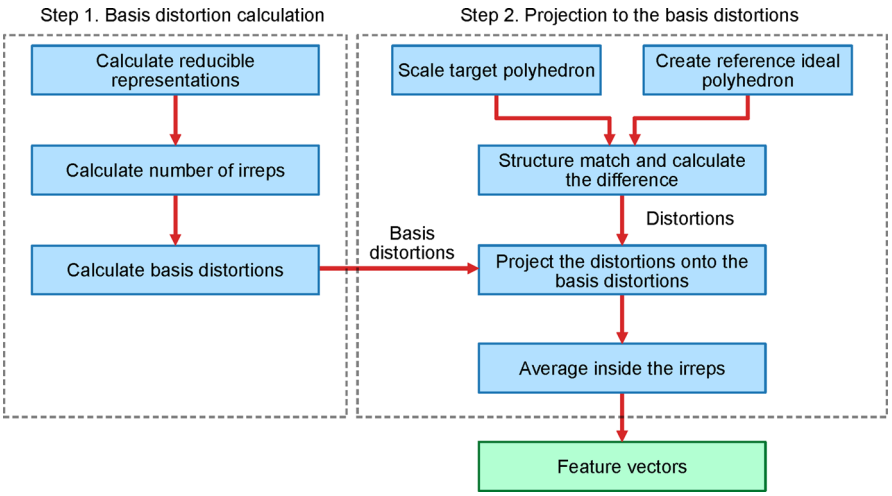

Figure 1. Flowchart of the structure featurization process. The coordinates of the polyhedron are taken as an input, and the feature vectors are returned.

coordination numbers. Although the coordination number is an intuitive concept, several different approaches have been suggested for a quantitative definition.[22−25] One advanced method is to analyze the connectivity of atoms and use the polygon created by the bonds to categorize the environment.[26,27] Other methods such as Smooth Overlap of Atomic Positions (SOAP), Coulomb matrix, Many-Body Tensor Representations (MBTR), or minimum bounding ellipsoid (MBE) have been suggested, which are based on atomic positions and do not rely on knowledge of the bonding network.[28−31]

Group theory serves as an important tool to interpret the underlying symmetry relations of crystal structures.[32−37] For example, Howard and Stokes exhausted the space groups accessible from cubic perovskites through rigid octahedral tilting.[38] More recently, Wagner et al. analyzed density functional theory (DFT) results using a combination of group theory and statistical correlation analysis and showed the efficacy of combining these techniques.[39] Not only in theoretical analyses, but also in experiments, group theoretical techniques are used to determine crystal structures, which is a challenging task in some cases and, therefore, beoming an actively developing research field.[40]

In this paper, we take advantage of established techniques in group theory and use them to encode polyhedron shapes. In particular, we projected the distortions onto the basis vectors of the irreducible representations (irreps) to obtain a physically intuitive decomposition of the distortions. The obtained expression is atomic permutation invariant, axis invariant, minimum length, and physically transparent, meeting all criteria for a suitable material representation for training statistical models. Although our method is applicable to any type of polyhedron, we chose octahedra inside perovskite-type materials as a model system, as it is well studied.[41−47] We show that our approach, when applied to these classes of materials, not only rediscovers intuitively understandable behavior but is also capable of capturing trends that originate from subtle differences in an octahedral geometry.

METHODOLOGY

The overview of the featurization process is schematically presented in Figure 1. The process is largely split into two parts: the basis distortion calculation and the projection of the distortions onto the basis. In the first step, basis distortions corresponding to the irreps are computed using group theoretical techniques. Next, the distortions of the target polyhedra are calculated with respect to the ideal aristotype polyhedron, and the distortions are projected onto the basis distortions calculated in the previous step. The explicit isolation of the first step allows it to be precomputed, thus minimizing the overall computational cost when applied to large data sets.

Basis Distortion Calculation. The first goal is to calculate complete and orthogonal basis distortions (basis vectors) of the irreps. The irreps fulfill the "great orthogonality theorem",[48]

$$\sum_R \Gamma^{(i)}(R)_{\mu\nu}\Gamma^{(j)}(R)_{\alpha\beta} = \frac{h}{l_i}\delta_{ij}\delta_{\mu\alpha}\delta_{\nu\beta} \tag{1}$$

Here, $\Gamma^{(i)}(R)_{\mu\nu}$ is a μ, ν matrix element of operator R in the irrep i, h is number of group elements, and l_i is the dimensionality of $\Gamma^{(i)}$. We cannot directly use this, however, because the specific elements of Γ are unknown *a priori*. Therefore, throughout the section, we make use of their trace or their character, which are readily available from standard character tables. We will use the six-atom octahedron geometry as an example, but our method is applicable to all symmetric coordination environments. The notation follows that in ref 48.

First, we need to calculate 18-dimensional reducible representations, which is a direct product between a six-dimensional atomic site and three-dimensional vector representations. The three-dimensional representations $\tilde{\Gamma}^{(3)}(R)$ (tilde indicating a reducible representation) are readily available from previous studies, in which we have adopted them from the *phonopy* package.[49] On the other hand, six-dimensional representations $\tilde{\Gamma}^{(6)}(R)$ depend on specific problems; therefore, we have calculated them by applying the three-dimensional representation $\tilde{\Gamma}^{(3)}(R)$ to atomic coordinates and keeping track of which atoms transformed to which atomic sites. The final 18-dimensional representations $\tilde{\Gamma}^{(18)}(R)$ were constructed by taking a tensor product between three- and six-dimensional representation $\tilde{\Gamma}^{(3)}(R) \otimes \tilde{\Gamma}^{(6)}(R)$.

https://doi.org/10.1021/acs.chemmater.1c02959
Chem. Mater. 2022, 34, 562−573

Second, we calculate the number of irreps hidden within the 18-dimensional reducible representation $\tilde{\Gamma}^{(18)}(R)$. To do this, we use the following equation,

$$\sum_R \chi^{(i)}(R)\chi^{(j)}(R) = \frac{h}{l_i}\delta_{ij} \tag{2}$$

Here $\chi^{(i)}$ is a character of irrep $\Gamma^{(i)}$, which is calculated by taking a trace. Although this relation is simply derived by taking the trace of eq 1, it is useful in our case, since it does not require knowledge of specific elements of irreps, while the characters are known (Table S1). Since $\tilde{\chi}^{(18)}(R) = \sum_i a_i \chi^{(i)}(R)$, where a_i is the number of irreps i in 18-dimensional representation, eq 2 could extract a_i. The calculated result for an octahedron is shown in Table 1. We can see that there are one A (one-dimensional), one E (two-dimensional), and four T's (three-dimensional), which add up to the 18 total degrees of freedom in the system.

Table 1. Number of Irreducible Representations in 18-Dimensional Reducible Representation in O_h Symmetry

A_{1g}	A_{2g}	E_g	T_{1g}	T_{2g}	A_{1u}	A_{2u}	E_u	T_{1u}	T_{2u}
1	0	1	1	1	0	0	0	2	1

Finally, we calculated the basis vectors. To do so, we have used the "basis-function generating machine",[48] which is defined as

$$\mathcal{P}^{(i)}_{\lambda\kappa} := \frac{l_i}{h}\sum_R \Gamma^{(i)}(R)_{\lambda\kappa} P_R \tag{3}$$

where P_R is the projection operator of symmetry operator R. The useful property of $\mathcal{P}$ is that when it is operated on an arbitrary function

$$F := \sum_i \sum_\kappa^{l_i} f^{(i)}_\kappa \tag{4}$$

it could take out $f^{(i)}_\kappa$, the κth element within irrep i of the function F

$$\mathcal{P}^{(i)}_{\kappa\kappa} F = f^{(i)}_\kappa \tag{5}$$

Again, a problem arises due to a lack of knowledge on $\Gamma^{(i)}(R)$. Analogously to the relation between eq 1 and 2, there is a slightly restricted version,[50] which is

$$\mathcal{P}^{(i)} := \frac{l_i}{h}\sum_R \chi^{(i)}(R) P_R \tag{6}$$

$$\mathcal{P}^{(i)} F = \sum_\kappa f^{(i)}_\kappa \tag{7}$$

The difference is that we could only resolve up to an irrep, and components inside an irrep κ remain degenerate. Our approach for deciding the basis set inside multidimensional irreps was to generate arbitrary vectors within an irrep and use Gram–Schmidt orthogonalization to decompose them into orthogonal basis vectors.

Specifically, for each irrep within Table 1, we arbitrarily chose a vector residing on an atom, subsequently applied all the symmetry operators, and multiplied the character corresponding to the irrep. The projected results were then added, which resulted in a basis set, as in eq 6. This step was repeated three times with unit vectors in x, y, and z directions. Although the number of trial initial vectors is arbitrary, this choice is the minimum number required to generate all irreps. We then removed duplicates and zero vectors and further applied Gram–Schmidt orthogonalization,

$$\psi^{(i)}_\kappa = \psi'^{(i)} - \sum_{\lambda\neq\kappa}^{l_i} (\psi'^{(i)}\cdot\psi^{(i)}_\lambda)\psi^{(i)}_\lambda \tag{8}$$

where $\psi'^{(i)}$ is an unorthogonalized vector residing in irrep i and λ runs over other basis set within irrep i that is not κ. Lastly, we have normalized the vectors such that their inner product with themselves equal unity.

Although this method is systematic, one arbitrary choice is the initial vectors for eq 6. In principle, we could use three unit vectors in different directions and still obtain an irrep. We will later show that we decided to average over dimensions, and such averaging is necessary even if we have used the full basis set generating machine in eq 3. Following this procedure produces a complete and orthogonal basis set for the irreps which describe all the possible displacements of atoms in an

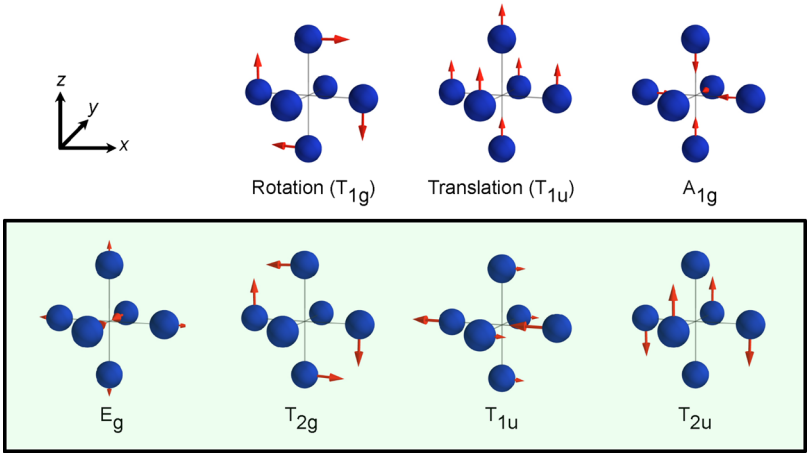

Figure 2. Basis set distortions for the irreducible representations of a six atom octahedron as found in a cubic perovskite. For multidimensional irreducible representations, only one distortion is shown. For the actual projection, we have used the four distortions presented in the bottom row. The full list is presented in Figures S1 and S2.

https://doi.org/10.1021/acs.chemmater.1c02959
Chem. Mater. 2022, 34, 562−573

octahedron. The representative distortions are presented in Figure 2 (full list in Figures S1 and S2).

Projection to the Basis Distortions. The projection of an arbitrary structure on this basis set was performed in three steps: normalization, structure matching, and distortion amplitude averaging.

If we simply project two distorted octahedra with the same shape but different sizes, we will obtain different distortion amplitudes. This is not favorable in the context of analyzing the shape of the octahedra. Therefore, some kind of normalization of the input octahedron is necessary. Our approach was to scale the distorted octahedron such that the average bond length is 1.0 Å and obtain the distortion vector by comparing it against the ideal octahedron with a bonding length of 1.0 Å. By applying this scaling, the resulting distortion amplitudes for octahedra of the same shape but different sizes became identical.

Although our method is permutation invariant, practically, we have to label atoms within the code. Therefore, to calculate the distortions the atomic indices of the distorted and the ideal octahedron must be matched. This structure matching requires $O(N!)$ computational cost, if calculated rigorously by brute-force algorithm, but we found that this is too slow for high-throughput applications. To make the computational cost feasible, we employed the Hungarian algorithm, as implemented in the *pymatgen* package.[51,52] We confirmed that this algorithm works well in perovskites and perovskite-related materials, which typically have well-defined octahedra; however, for geometry with large variation in bonding length, brute force algorithms are likely to be favored. After matching the structure, the distortion vectors were calculated and were projected onto basis vectors presented in Figure 2. Furthermore, we have validated the quality of this basis by reconstructing the original distortion from the projection and confirmed that the error is negligible (Figure S3).

It is tempting to use the amplitudes we have obtained above directly; however, the raw values encompass the aforementioned arbitrariness within the multidimensional irreps, which originates from the usage of eq 6 rather than eq 3. Taking a closer look, the choice of basis vectors within a single irrep follows a rotational group or special orthogonal group. Since the actual configuration of an input octahedron inside a crystal may be rotated in any possible direction, even if we have used the full basis set generating machine (eq 3), the resulting amplitudes of the basis vectors would have had a dependence on the choice of the axis. For example, if the T_{1u} distortion in Figure 2 is rotated 90° about the x axis, the amplitudes obtained by projection onto the original T_{1u} distortion and the transformed T_{1u} will be different. This situation is encountered in all the distortions except for A_{1g}, which has no multiplicity and is thus rotational invariant. Therefore, the arbitrariness due to a dependence of rotation is a problem that exists regardless of whether or not we use eq 6. Since one of the purposes of this analysis is to obtain ML-friendly features, rotational variance is not favorable, especially because for a typical ML model, learning a permutation is a challenging task.[53]

Our approach was to use the total length spanned by vectors within the irreps. As shown in Figure 3, we have calculated the length of the vectors in two- or three-dimensional space using the Euclidean norm,

$$\Phi^{(i)} = \sqrt{\sum_{\kappa} \psi_{\kappa}^{(i)} \cdot \psi_{\kappa}^{(i)}} \tag{9}$$

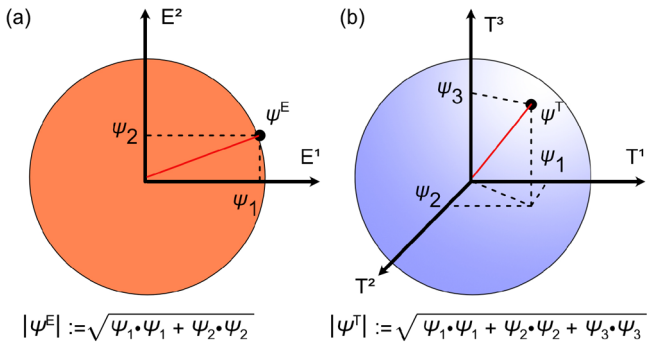

Figure 3. Illustration of how amplitudes are averaged within a multidimensional irreducible representation. (a) Two-dimensional irreducible representation (E_g) and (b) three-dimensional irreducible representations (T_{2g}, T_{1u}, and T_{2u}).

Here the summation is over the dimension inside irrep (i). Just like how the Euclidean distance of a given point from the origin remains the same under rotations about the origin, this expression is invariant under any orthogonal transform. Another interpretation of this approach is that we are rotating the axis in Figure 3, so that one of the axes is aligned with the amplitude vector and then reading the value off that axis.

Through the above procedures, we were able to obtain a scalar value for each irrep for any distorted octahedron. Lastly, translation, rotation, and scaling distortions (A_{1g}) were discarded, since they do not have information regarding the shape of the octahedron. We note that it is possible to encode information such as rigid shifting, rigid tilting, or octahedron size into these irreps, but it will require modification to the structure matching procedure and is likely to introduce additional complexity in the algorithms. Therefore, we report four scalar values each corresponding to E_g, T_{2g}, T_{1u}, and T_{2u} for rest of the work.

Lastly, it is worth mentioning extension to other polyhedra. One of the simpler but yet often encountered geometries in materials science is the tetrahedron. Since a tetrahedron has four vertices, the total degrees of freedom will be 12, of which seven belong to translation, rotation, and scaling distortions. The remaining five are E and T_2 distortions, which are averaged within the irrep and used as a feature. In this case, the feature may be too small to be used to train an ML model solely, but at the same time, this indicates that the variation in the shape of a tetrahedron is residing in much smaller dimensions compared to the case of an octahedron. Another abundant geometry is the cuboctahedron, which is seen, for example, in the A-site of perovskites. The total degree of freedom is 36, and removing translation, rotation, and scaling distortions will retain A_{2g}, two E_g, T_{1g}, two T_{2g}, A_{2u}, E_u, two T_{1u}, and two T_{1u} distortions. Depending on the application, this dimensionality may be directly used to train ML models, but in practice, if the analysis is restricted to certain classes of materials, we speculate that some of the distortions would not be present and could be removed by using feature selection techniques, such as *k highest score*.[54]

Data Set Processing. To apply the projection, we have obtained 46 048 materials from the *Materials Project* database (accessed on 27/06/2020) through the API in the *pymatgen* package.[52,55,56] We then applied the *CrystalNN* algorithm to obtain coordination number and environment for all the atomic sites. We have selected ABO_3 stoichiometry materials containing 6-fold coordinated cations. In theory, there may be

https://doi.org/10.1021/acs.chemmater.1c02959
Chem. Mater. 2022, 34, 562−573

6-fold coordinated atomic sites without an octahedron geometry, but we did not observe such a case within our curated data set. For materials containing multiple symmetry inequivalent octahedra, we have detected them according to their Wyckoff positions with the *spglib* library.[57] The inequivalent sites were treated as independent data, which resulted in 552 distinct octahedra in total. For a given composition, there are multiple structures, and we have not explicitly taken into account their thermodynamic stability. Therefore, our analysis contains structures that may not have been synthesized to date but represent local minima on DFT potential energy landscapes.

Density Functional Theory Calculations. Although we have largely applied the method to openly available data from the *Materials Project* database,[52,55,56] for validation we performed some calculations with stricter conditions. The plane-wave DFT calculations within projector-augmented wave scheme were performed using the *VASP*.[58−60] The input file was automatically generated via *VISE* package,[61] resulting in cutoff energy of 520 eV and the reciprocal space sampling of at least $2\pi \times 0.05$ Å^{-1}. Using the structures in the *Materials Project* as an initial input, the cell size and the atomic coordinates were fully relaxed using the HSE06 exchange-correlation functional.[62,63] The visualization of structures was done using *VESTA*.[64]

Predicting Potential Energy. To demonstrate applicability of our featurization procedure toward supervised machine learning of materials, we trained an ML model to predict potential energy generated by Born−Oppenheimer molecular dynamics (BOMD) of $CsPbI_3$. The unit cell was expanded into a $2 \times 2 \times 2$ pseudocubic supercell following previous studies.[65,66] Using *VASP*, the 300 K NVT ensemble calculation was computed with cutoff energy of 400 eV, the reciprocal space sampling of $3 \times 3 \times 3$, the time step of 0.4 fs, and PBEsol exchange-correlation functional.[62,67] The system was equilibrated for 15 000 steps, and a production run was performed for 39 000 steps with sampling taken every 50 steps, which resulted in 780 data points.

For each snapshot, octahedral distortions were featurized, normalized with robust scaler, and shuffled randomly. The preprocessed features were fed into support vector regression (SVR), as implemented in the *scikit-learn* library, and trained to predict the potential energy.[54] For the kernel, the radial basis function (RBF) kernel was employed. Fivefold cross-validation was used to optimize hyperparameters resulting in kernel coefficient γ of 0.1 and regularization parameter (variable C in *scikit-learn*) of 1.0.

RESULTS AND DISCUSSION

Projection onto Normal Distortions. The distribution of distortion amplitudes for all 552 materials is presented in Figure 4. The materials are categorized by whether or not they belong to the common corner-shared perovskite space group (cubic $Pm\bar{3}m$, tetragonal $P4mm$, tetragonal $P4/mmm$, tetragonal $P4/mbm$, tetragonal $I4/mcm$, orthorhombic $Pnma$, orthorhombic $Amm2$, orthorhombic $Cmcm$, monoclinic $P2_1/m$, rhombohedral $R3m$, rhombohedral $R3c$, and rhombohedral $R\bar{3}c$).[38] The numbers of materials in common and uncommon space groups were 443 and 109, respectively. From Figure 4, differences in the distributions are clearly noticeable for the two classes of materials. For the common space groups, the vast majority had little or no distortion, and the number of materials decay monotonically with increasing amplitudes. In contrast, for less common space groups, the distribution exhibited a wider spread, and the larger portion of materials had larger amplitudes. Additional peaks are clearly seen for T_{2g} and T_{1u} around 0.075 and 0.100, respectively. Accounting for the fact that there were no clear chemical trends (Figures S4−S7), this result suggests a strong relationship between the crystal structure and the local distortions of the octahedra.

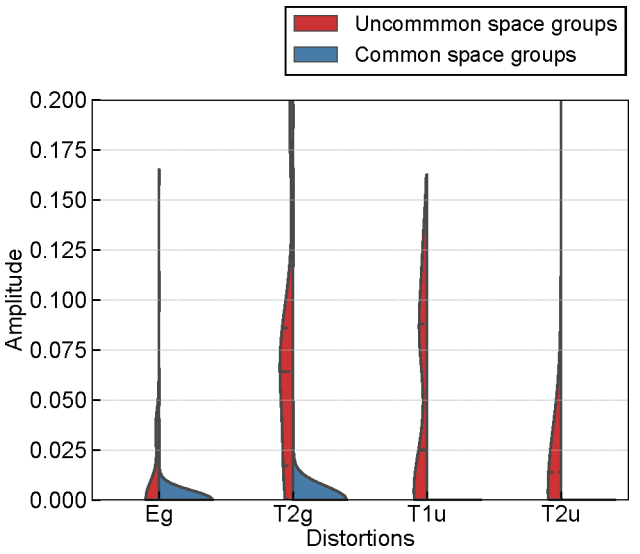

Figure 4. Distortion amplitudes for 552 ABO_3 octahedra from 492 materials. The blue and red shading refers to materials that belong or do not belong to the common space groups for distorted corner-sharing perovskites, respectively.

Connectivity Analysis. To analyze the underlying material trends in more detail, we have plotted the T_{1u} distortion against the T_{2g} distortion and categorized each site according to their connectivity with neighboring octahedra (Figure 5).

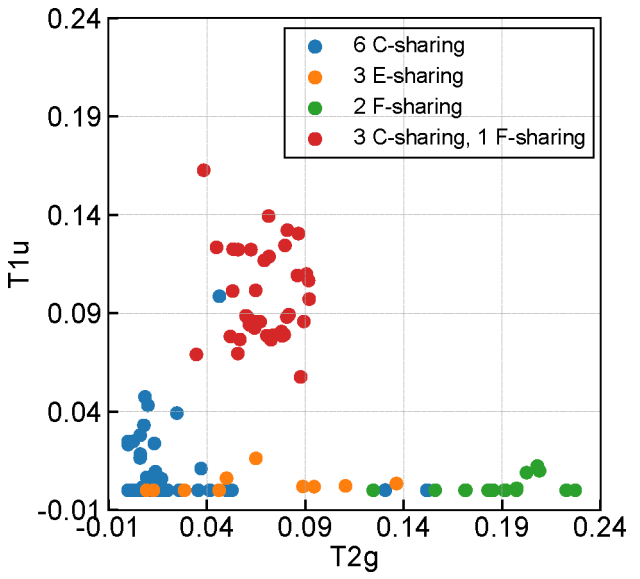

Figure 5. Relation between T_{1u} distortion against the T_{2g} distortion. Each point represents an octahedron site and is colored according to its connectivity with other octahedra. Blue points are connected via six corner-sharing (6 C-sharing), orange points are connected via three edge-sharing (3 E-sharing), red points are connected via three corner-sharing and one face-sharing (3 C-sharing and 1 F-sharing), and green points are connected via two face-sharing (2 F-sharing).

https://doi.org/10.1021/acs.chemmater.1c02959
Chem. Mater. 2022, 34, 562−573

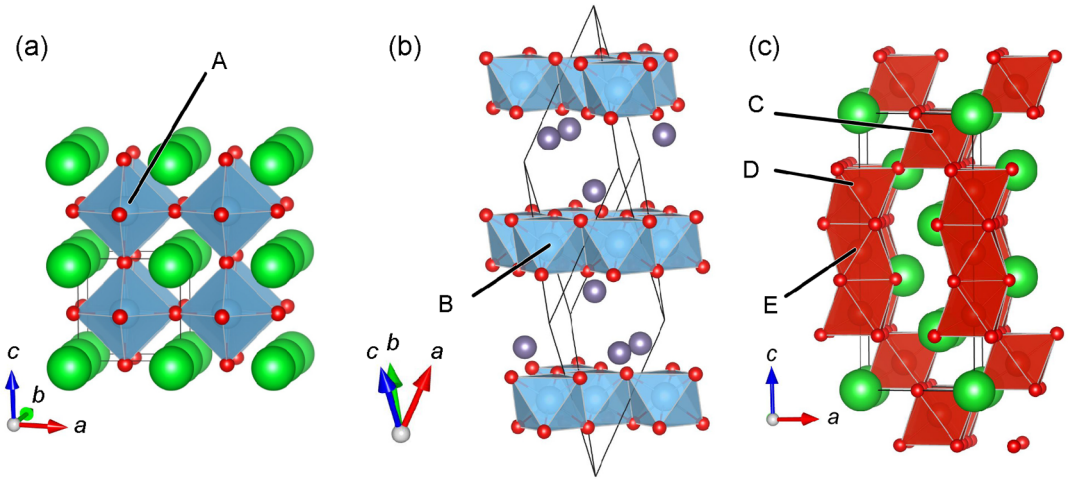

Figure 6. Structures of (a) cubic $SrTiO_3$, (b) rhombohedral $GeTiO_3$, and (c) hexagonal $BaVO_3$. Octahedra are composed of TiO_6, TiO_6, and VO_6, respectively. Distinct Wyckoff positions are labeled with A to E.

The connectivity was obtained by counting how many oxygen atoms are shared with neighboring octahedra, accounting for periodic boundary conditions. The four connectivities in Figure 5 are six corner-sharing (6 C-sharing, A and C in Figure 6), three edge-sharing (3 E-sharing, B in Figure 6), two face-sharing (2 F-sharing, E in Figure 6), and three corner-sharing and one face-sharing (3 C-sharing and 1 F-sharing, D in Figure 6).

A cluster of distortion amplitudes is distinguishable at about (T_{2g}, T_{1u}) = (0.075, 0.100). Two interesting observations could be made from this clustering. The first is that T_{1u} distortion amplitude of over 0.05 is only present in this cluster. This suggests that the large amplitude of T_{1u} distortions could only exist when T_{2g} distortions coexist. The behavior is analogous to improper ferroelectrics where the coexistence of two distortions creates a ferroelectric distortion.[68−70] Second, this cluster is composed mostly of three corner-sharing and one face-sharing connectivity. This type of octahedral connectivity is realized in hexagonal perovskite polytypes where a 1D chain of face-sharing octahedra terminates as in Figure 6c. Accounting for the fact that three corner-sharing and one face-sharing octahedron were not seen outside of this cluster, this result indicates that hexagonal phases could support distortions much larger than that seen in corner-shared perovskites. The one fully point-shared outlier in the cluster was $BiFeO_3$, which exhibited an unusually large distortion. The possible origin of the large distortion is the stereochemical activity of the Bi lone pair, as suggested by previous studies.[71−73]

Outside of this cluster, the T_{1u} distortion was generally small. Most of the fully corner-shared octahedra and fully edge-sharing octahedra possess an ideal structure, which made the data points scattered around the zero amplitude point. Two face-sharing octahedra, interestingly, had a very large T_{2g} distortion but lacked T_{1u}. Since this connectivity occurs in the middle of a 1D chain in hexagonal phases as in site E in Figure 6, the uniaxial strain due to being sandwiched by neighboring octahedra is likely to have caused the compression of the octahedron.

Clustering Analysis. Up to here, we have made discussions based on the trends in Figure 5; however, such a discussion may be overlooking trends in higher dimensions. Therefore, we performed dimensionality reduction analysis to understand the clustering of different octahedral connectivities in higher dimensions. We employed t-distributed stochastic neighbor embedding (t-SNE) to perform nonlinear reduction from four to two dimensions.[74,75] The result is shown in Figure 7. Different octahedral connectivities are clearly separated.

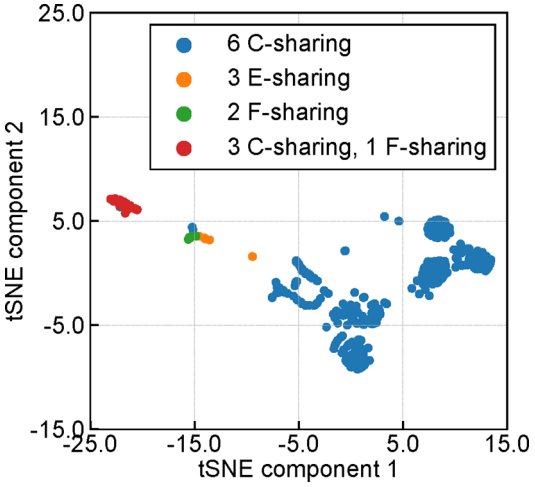

Figure 7. Clustering of different octahedron connectivities plotted on the dimensionally reduced axis obtained through t-distributed stochastic neighbor embedding (t-SNE).

This result is fortuitous since it indicates that the shape of octahedra is largely determined by their connectivities with neighboring octahedra. In other words, a geometrical network of bonds dominantly determines the shape of the octahedra rather than the chemical property of individual bonds. The two fully corner sharing (6 C-sharing) outliers near the face sharing (2 F-sharing) cluster were $TeCoO_3$ and $TeMnO_3$ (filed as $CoTeO_3$ and $MnTeO_3$ in the *Materials Project*, respectively). The large distortions in these materials are realized by covalent interaction between tellurium and oxygen and due to strong tellurium lone pairs.[76] $BiFeO_3$ seen in Figure 5 also appears again as an outlier within the 3 C-sharing and 1 F-sharing cluster.

We next perform a clustering analysis in the full four-dimensional space to see if there is additional information to be obtained. The multidimensional clustering was analyzed by

https://doi.org/10.1021/acs.chemmater.1c02959
Chem. Mater. 2022, 34, 562−573

a Gaussian mixture model (GMM).[75] GMM requires a number of clusters to be set *a priori*; therefore, we calculated the minimum number of clusters needed to account for the data using the information criteria analysis and selected nine clusters to be adequate (Figure S12). The obtained nine clusters are presented in Figure 8 (plot against all axes are shown in Figure S13). It should be noted that, in GMM, a data point could only belong to a single cluster. In Figure 8a, a clear ellipsoid of cluster 0 can be distinguished. This cluster corresponds to the three corner-sharing and one face-sharing in Figure 5 at $(T_{2g},T_{1u}) = (0.075, 0.100)$. A closer look reveals that there is a subset of materials within the ellipsoid that belong to cluster 5. Their difference is not distinguishable from Figure 8a, but plotting against the T_{2u} distortion axis in Figure 8b reveals that cluster 5 is displaced from cluster 0 in the T_{2u} distortion axis. Cluster 0 had no T_{2u} distortions, whereas cluster 5 had about 0.02 T_{2u} distortion. This separation is not trivial from Figure 5 and highlights the value of clustering analysis in the high dimensional space. We will discuss specific constituent materials of cluster 5 next.

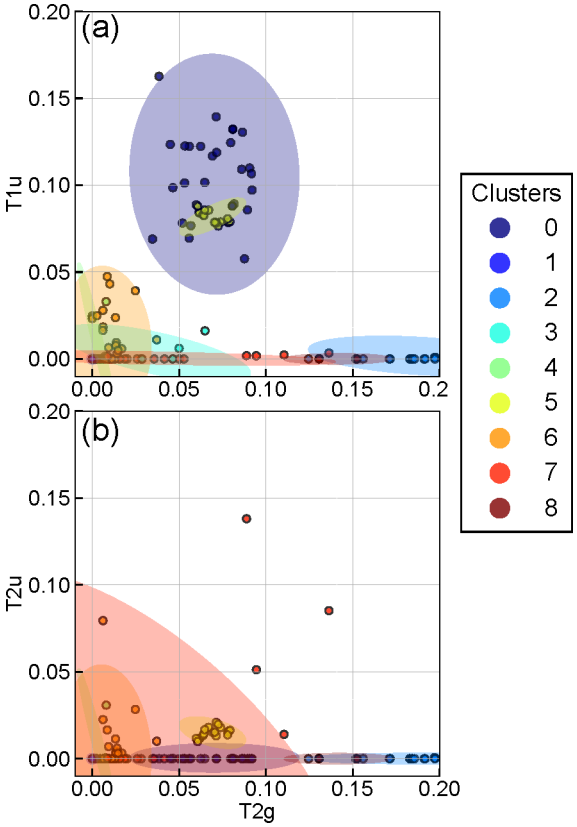

Figure 8. Clusters obtained by a Gaussian mixture model shown in the axis of (a) T_{2g} and T_{1u} and (b) T_{2g} and T_{2u}. The dots are colored differently depending on which of the seven different clusters the point belongs to. The shading shows the extent of the multivariate Gaussian distribution defined for each cluster.

Analysis of Specific Materials. Cluster 5 in Figure 8 is mainly composed of $BaTiO_3$ and different polymorphs of $SrCrO_3$. We find that the distortions in $BaTiO_3$ were typical for hexagonal phases. Within our data set, there were two polymorphs of hexagonal $BaTiO_3$, the $C222_1$ phase and the $P6_3/mmc$ phase (Figure 9a,b, respectively). Experimentally, $C222_1$ is stable in the range of about 70−220 K, where it transforms into the $P6_3/mmc$ phase at 220 K.[77,78] The low temperature $C222_1$ phase has the T_{2u} distortions, but they are averaged out and are absent in the high temperature $P6_3/mmc$ phase. The structural difference between the $C222_2$ and the $P6_3/mmc$ phases is presented in Figure 9c.

To confirm whether the absence of the T_{2u} distortions in other ABO_3 structures is due to the lack of data or due to different phase stability, we have compared the energies of the $P6_3/mmc$ and $C222_1$ phases in 11 additional compounds (Table 2). We found that in most compounds the $C222_1$ phase was stable, suggesting it to be the lower temperature phase, thus showing that the $BaTiO_3$ with finite T_{2u} is not exceptional but rather a property of hexagonal phase materials. The exceptions were $SrCrO_3$, $BaCrO_3$, and $BaRuO_3$. The energy differences in $BaCrO_3$, and $BaRuO_3$ were subtle, but $SrCrO_3$ had clearly higher stability of the $P6_3/mmc$ phase.

$SrCrO_3$ is an interesting case that has an interplay of metallicity, ferroelectricity, and magnetic order. In cubic $SrCrO_3$, there have been reports on multiferroicity, which are induced by orbital ordering.[20,79,80] Since this material has been suggested to be internally strained,[81] we believe this is the

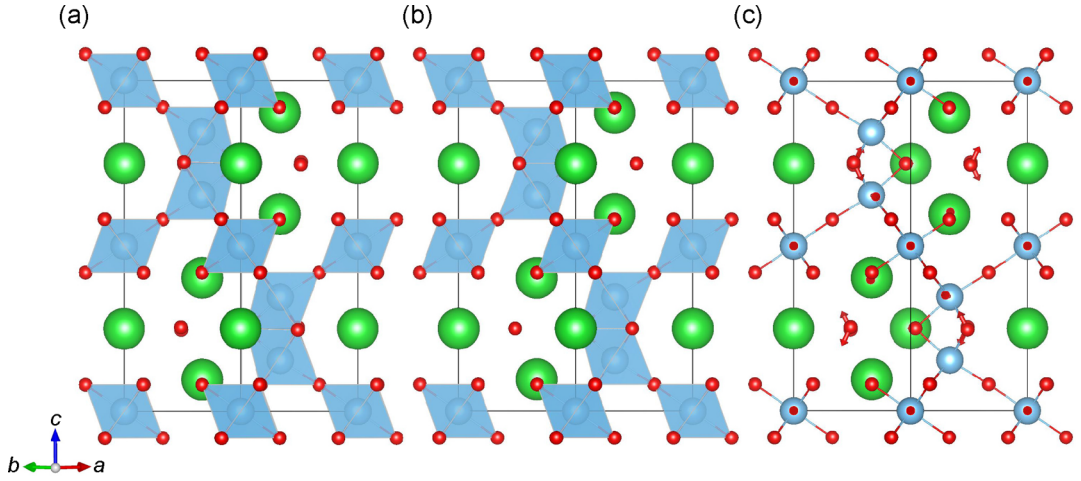

Figure 9. Structure of $BaTiO_3$ in the (a) $C222_1$ and (b) $P6_3/mmc$ phases. (c) Atomic displacement to transform from $C222_1$ to $P6_3/mmc$. The blue, green, and red spheres are Ba, Ti, and O atoms, respectively. The blue shading represents the TiO_6 octahedron.

https://doi.org/10.1021/acs.chemmater.1c02959
Chem. Mater. 2022, 34, 562−573

Table 2. Calculated Relative Stability (DFT/HSE06) of the Low Temperature $C222_1$ Phase Compared to the High Temperature $P6_3/mmc$ (See Illustration in Figure 9)

compound	$E_{P6_3/mmc} - E_{C222_1}$ (meV/atom)
$CaTiO_3$	18.61
$CaCrO_3$	61.56
$CaMnO_3$	30.08
$SrTiO_3$	3.88
$SrCrO_3$	−16.11
$SrMnO_3$	5.18
$BaTiO_3$	0.72
$BaVO_3$	37.31
$BaCrO_3$	−6.29
$BaMnO_3$	10.34
$BaRuO_3$	−1.11
$BaRhO_3$	4.68

reason for the distinct distortion behavior of this material. For hexagonal polytypes of $SrCrO_3$ (Figure 10), which have not been reported to the best of our knowledge, we note that the formation energy predicted by DFT is smaller than that of the known cubic phase (Table S2), which suggests that they should be accessible. Interestingly, within the hexagonal phases, the *Ama*2 phases (Figure 10a−c) were calculated to be metallic, whereas the $P6_3/mmc$ phases (Figure 10e,f) were insulators (Table S2). For polymorphs without a band gap, we have confirmed their metallicity with our DFT/HSE06 calculations. Since the ratio of corner-shared and face-shared connectivities could be controlled by the stacking sequence, we speculate that, through the tuning of the polytype order, metallicity/insulating, ferroelectricity/paraelectricity, and ferromagnetic/paramagnetic behavior could be accessed. Furthermore, like orbital ordering observed for the cubic phase, coupling of different behaviors is also expected here.

Application to Supervised Learning. In addition to the material discovery problem demonstrated above, our featurization method could also be applied to thermodynamic problems. We generated a data set of potential energy for snapshots obtained from the BOMD calculation of $CsPbI_3$ and used it to train an SVR model. We have chosen potential energy as it only depends on the atomic coordinates and serves as a good benchmark to assess the capability of capturing thermally induced lattice distortions. The featurization

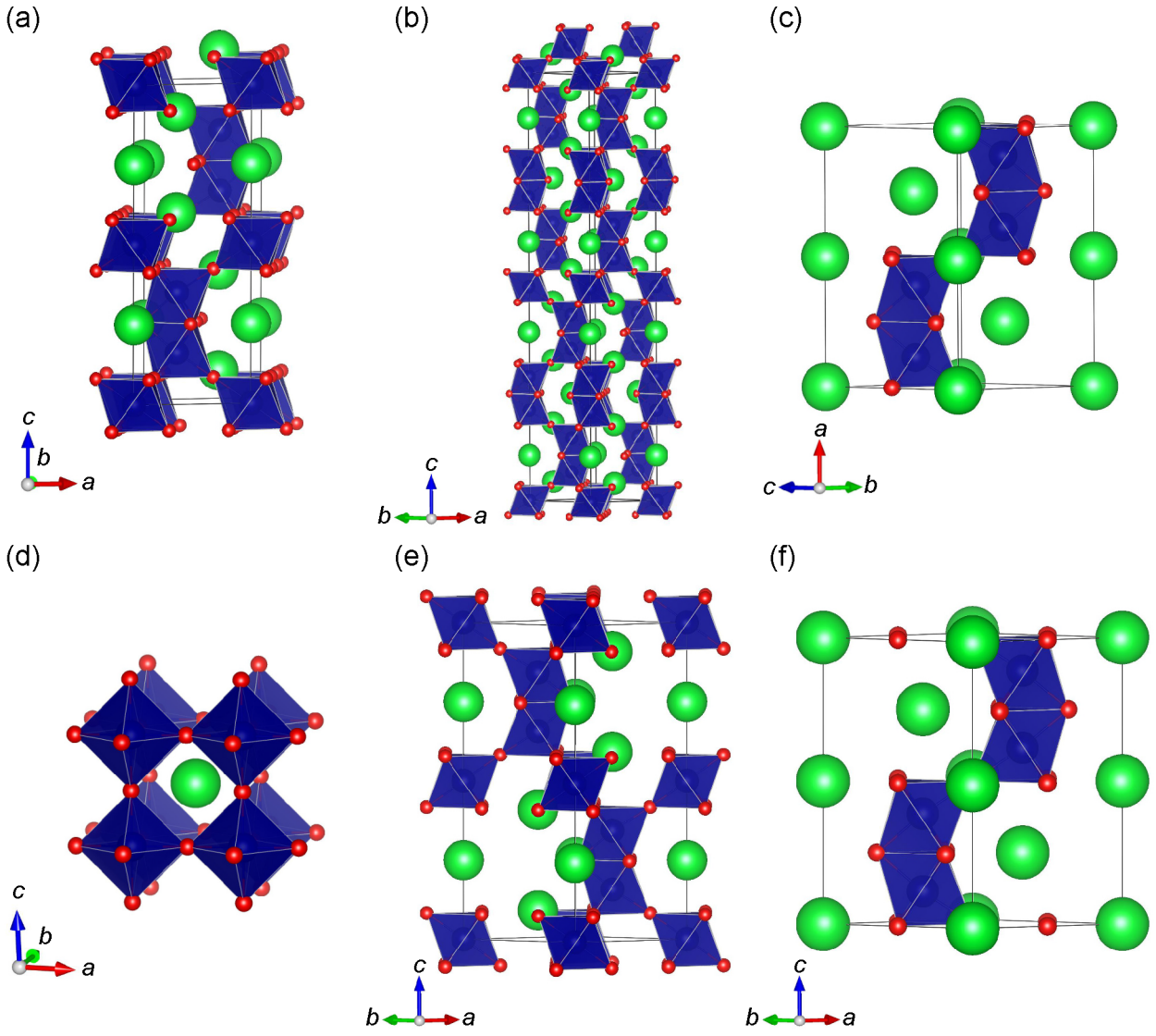

Figure 10. Structures of different $SrCrO_3$ polymorphs. The details are summarized in Table S2.

https://doi.org/10.1021/acs.chemmater.1c02959
Chem. Mater. 2022, 34, 562−573

procedure was the same as above, except we also make the use of A_{1g} distortions relative to the 0 K geometry optimized structure. Since there were eight octahedra in the calculation cell as shown in Figure 11a, the dimensionality of the feature

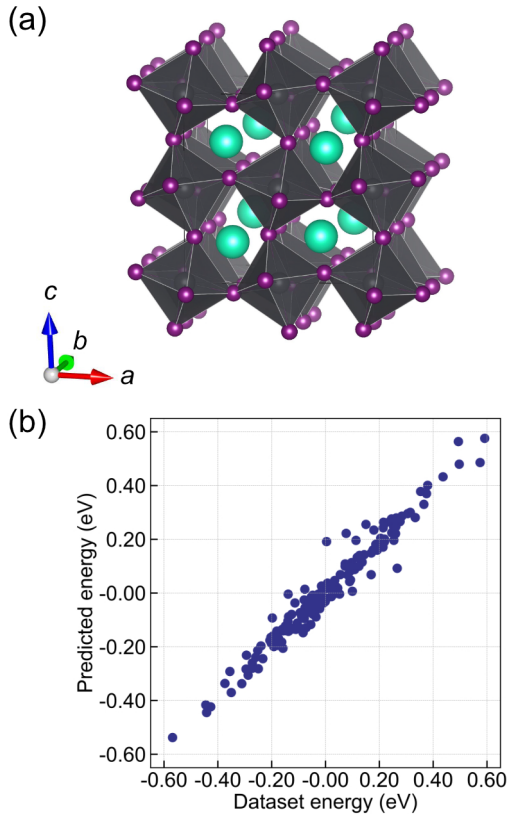

Figure 11. (a) Pseudocubic $CsPbI_3$ 2 × 2 × 2 supercell used for the molecular dynamics simulation. The gray octahedra with purple vertices are PbI_6, and the teal spheres are Cs. (b) Comparison between the data set and the support vector regression prediction of the potential energy test data.

was 40. This is a good example of a case where the scaling distortion could be used to incorporate the domain knowledge of the problem. Figure 11b shows the SVR prediction of the test data with the zero of the energy set to be the average potential energy during the BOMD simulation (raw values shown in Figure S15). The r^2 and mean absolute error for the test (training) data were 0.956 (0.989) and 31.2 meV (18.2 meV), respectively. The high accuracy is notable considering the model contains no explicit information regarding the atomic positions of Cs and Pb. We believe that since Pb and Cs are heavier, the displacement is smaller and thus the change in the interatomic distances could dominantly be taken into account by considering I. Since this is a finite temperature calculation, given a configuration of I, there are numerous possible positions of Cs and Pb, so such a degree of freedom is likely to be a reason for some of the outliers seen in Figure 11b. We therefore expect increasing error with temperature. This result shows the efficiency of the featurization method toward supervised learning.

Discussion on Other Applications. Comparing our method to other types of local structural featurization, conventional methods that incorporate basis set expansion of the local environment will capture a wider variety of environments and may be better suited for training general purpose machine-learned force fields that could describe solid−liquid transitions, for example. In contrast to their generality, these types of expansions typically have orders of magnitude larger feature size, ∼1000 for SOAP,[82] which require significant data and training times. Furthermore, in such high dimensional methods, the features are not guaranteed to correspond directly with the displacement of atoms and thus may obstruct analyses based on conventional symmetry arguments.[82] Our approach will have an advantage in encoding polyhedral distortions in cases where the data set size is not large enough to train general featurization techniques. A similar discussion holds when compared with graph neural networks, where our method has an advantage in smaller data sets.[83]

Like other approaches, our method is best suited for encoding local properties, but there are often cases where one wants to treat global properties. If the number of polyhedron sites is fixed throughout the data set, the features could be used directly, like in the BOMD analysis above. A problem occurs when a data set includes a variable number of polyhedron sites and in cases where the analysis method only accepts fixed-size input. The simplest solution is to use sum or average pooling. The choice between these two could be made by whether or not the property of the interest is intensive or extensive by nature.[8] The use of recurrent neural network based methods such as set2set could further improve the performance.[10]

CONCLUSION

We have shown that using a group theoric approach, distortions in polyhedra can be encoded into a small vector. As a case study, we have shown their efficacy toward representing the structures of ABO_3 stoichiometry oxides. In addition to recovering intuitively understandable trends, we presented the close relations between octahedra connectivity and their distortions, which are likely to be smeared out by some of the conventional analyses. As a coproduct, we were able to find $SrCrO_3$, which contained a rich variety of ferroic behaviors. We further showed that it is capable of predicting the potential energy of $CsPbI_3$ accurately with supervised machine learning. All of these analyses were performed solely on the information of the structures, and additional information such as thermodynamic stability and electronic structure will likely elucidate additional trends. We emphasize that this method is not exclusive, and synergistic effects are expected when combined with other featurization techniques. Finally, the results of this study are based on simple dimensional reduction analysis with the potential for further improvements using more sophisticated nonlinear approaches such as deep neural networks. We expect that these developments will open a path to more accurate statistical models and support further materials discoveries.

ASSOCIATED CONTENT

Supporting Information

The Supporting Information is available free of charge at https://pubs.acs.org/doi/10.1021/acs.chemmater.1c02959.

Detailed results on distortion analyses and density functional theory calculations omitted in the main text (PDF)

https://doi.org/10.1021/acs.chemmater.1c02959
Chem. Mater. 2022, 34, 562−573

AUTHOR INFORMATION

Corresponding Authors

Keith T. Butler − *SciML, Scientific Computer Division, Rutherford Appleton Laboratory, Harwell OX11 0QX, United Kingdom; Department of Chemistry, University of Reading, Reading RG6 6AD, United Kingdom;* orcid.org/0000-0001-5432-5597; Email: keith.butler@stfc.ac.uk

Aron Walsh − *Department of Materials, Imperial College London, London SW7 2AZ, United Kingdom; Department of Materials Science and Engineering, Yonsei University, Seoul 03722, Korea;* orcid.org/0000-0001-5460-7033; Email: a.walsh@imperial.ac.uk

Authors

Kazuki Morita − *Department of Materials, Imperial College London, London SW7 2AZ, United Kingdom;* orcid.org/0000-0002-2558-6963

Daniel W. Davies − *Research Computing Service, Information & Communication Technology, Imperial College London, London SW7 2AZ, United Kingdom*

Complete contact information is available at: https://pubs.acs.org/10.1021/acs.chemmater.1c02959

Notes

The authors declare no competing financial interest.

The code to perform the polyhedron analysis proposed in this study is freely available from https://github.com/KazMorita/polyhedron_distortion (latest version) or 10.5281/zenodo.5749806 (archived version).

ACKNOWLEDGMENTS

We thank funding support from Yoshida Scholarship Foundation, Japan Student Services Organization, and Centre for Doctoral Training on Theory and Simulation of Materials at Imperial College London funded by the EPSRC (EP/L015579/1). Via our membership of the UK's HEC Materials Chemistry Consortium, which is funded by EPSRC (EP/R029431), this work used the ARCHER2 UK National Supercomputing Service (http://www.archer2.ac.uk).

REFERENCES

(1) Alom, M. Z.; Taha, T. M.; Yakopcic, C.; Westberg, S.; Sidike, P.; Nasrin, M. S.; Esesn, B. C. V.; Awwal, A. A. S.; Asari, V. K. The History Began from Alexnet: A Comprehensive Survey on Deep Learning Approaches. *arXiv*, 2018, 1803.01164; https://arxiv.org/abs/1803.01164 (accessed December 14, 2021).

(2) Butler, K. T.; Davies, D. W.; Cartwright, H.; Isayev, O.; Walsh, A. Machine Learning for Molecular and Materials Science. *Nature* **2018**, *559*, 547−555.

(3) de Pablo, J. J.; et al. New Frontiers for the Materials Genome Initiative. *npj Comput. Mater.* **2019**, *5*, 41.

(4) Horton, M. K.; Dwaraknath, S.; Persson, K. A. Promises and Perils of Computational Materials Databases. *Nat. Comp. Sci.* **2021**, *1*, 3−5.

(5) Saal, J. E.; Oliynyk, A. O.; Meredig, B. Machine Learning in Materials Discovery: Confirmed Predictions and Their Underlying Approaches. *Annu. Rev. Mater. Res.* **2020**, *50*, 49−69.

(6) Musil, F.; Grisafi, A.; Bartók, A. P.; Ortner, C.; Csányi, G.; Ceriotti, M. Physics-Inspired Structural Representations for Molecules and Materials. *Chem. Rev.* **2021**, *121*, 9759−9815.

(7) George, J.; Hautier, G. Chemist versus Machine: Traditional Knowledge Versus Machine Learning Techniques. *Trends Chem.* **2021**, *3*, 86−95.

(8) Xie, T.; Grossman, J. C. Crystal Graph Convolutional Neural Networks for an Accurate and Interpretable Prediction of Material Properties. *Phys. Rev. Lett.* **2018**, *120*, 145301.

(9) Schütt, K. T.; Sauceda, H. E.; Kindermans, P.-J.; Tkatchenko, A.; Müller, K.-R. Schnet − A Deep Learning Architecture for Molecules and Materials. *J. Chem. Phys.* **2018**, *148*, 241722.

(10) Chen, C.; Ye, W.; Zuo, Y.; Zheng, C.; Ong, S. P. Graph Networks as a Universal Machine Learning Framework for Molecules and Crystals. *Chem. Mater.* **2019**, *31*, 3564−3572.

(11) Goodfellow, I.; Bengio, Y.; Courville, A. *Deep Learning*; MIT Press: 2016.

(12) Morita, K.; Davies, D. W.; Butler, K. T.; Walsh, A. Modeling the Dielectric Constants of Crystals Using Machine Learning. *J. Chem. Phys.* **2020**, *153*, No. 024503.

(13) Davies, D.; Butler, K.; Jackson, A.; Skelton, J.; Morita, K.; Walsh, A. Smact: Semiconducting Materials by Analogy and Chemical Theory. *JOSS* **2019**, *4*, 1361.

(14) Goodall, R. E. A.; Parackal, A. S.; Faber, F. A.; Armiento, R.; Lee, A. A. Rapid Discovery of Novel Materials by Coordinate-free Coarse Graining. *arXiv*, 2021, 2106.11132; https://arxiv.org/abs/2106.11132 (accessed December 14, 2021).

(15) Martin, L. W.; Rappe, A. M. Thin-Film Ferroelectric Materials and Their Applications. *Nat. Rev. Mater.* **2017**, *2*, 16087.

(16) Smith, M. B.; Page, K.; Siegrist, T.; Redmond, P. L.; Walter, E. C.; Seshadri, R.; Brus, L. E.; Steigerwald, M. L. Crystal Structure and the Paraelectric-to-Ferroelectric Phase Transition of Nanoscale $BaTiO_3$. *J. Am. Chem. Soc.* **2008**, *130*, 6955−6963.

(17) Zhang, X.; Liu, Q.; Luo, J.-W.; Freeman, A. J.; Zunger, A. Hidden Spin Polarization in Inversion-Symmetric Bulk Crystals. *Nat. Phys.* **2014**, *10*, 387−393.

(18) Nguyen, L. T.; Cava, R. J. Hexagonal Perovskites as Quantum Materials. *Chem. Rev.* **2021**, *121*, 2935−2965.

(19) Eerenstein, W.; Mathur, N. D.; Scott, J. F. Multiferroic and Magnetoelectric Materials. *Nature* **2006**, *442*, 759−765.

(20) Khomskii, D. I.; Streltsov, S. V. Orbital Effects in Solids: Basics, Recent Progress, and Opportunities. *Chem. Rev.* **2021**, *121*, 2992−3030.

(21) Batra, R.; Song, L.; Ramprasad, R. Emerging Materials Intelligence Ecosystems Propelled by Machine Learning. *Nat. Rev. Mater.* **2021**, *6*, 655.

(22) Hoppe, R. Effective Coordination Numbers (ECoN) and Mean Fictive Ionic Radii (MEFIR). *Z. Kristallogr. - Cryst. Mater.* **1979**, *150*, 23−52.

(23) Brunner, G. O. A Definition of Coordination and its Relevance in the Structure Types AlB_2 and NiAs. *Acta Crystallogr., Sect. A* **1977**, *33*, 226−227.

(24) O'Keefe, M.; Brese, N. Atom Sizes and Bond Lengths in Molecules and Crystals. *J. Am. Chem. Soc.* **1991**, *113*, 3226−3229.

(25) Zimmermann, N. E. R.; Jain, A. Local Structure Order Parameters and Site Fingerprints for Quantification of Coordination Environment and Crystal Structure Similarity. *RSC Adv.* **2020**, *10*, 6063−6081.

(26) Isayev, O.; Oses, C.; Toher, C.; Gossett, E.; Curtarolo, S.; Tropsha, A. Universal Fragment Descriptors for Predicting Properties of Inorganic Crystals. *Nat. Commun.* **2017**, *8*, 15679.

(27) Waroquiers, D.; Gonze, X.; Rignanese, G.-M.; Welker-Nieuwoudt, C.; Rosowski, F.; Göbel, M.; Schenk, S.; Degelmann, P.; André, R.; Glaum, R.; Hautier, G. Statistical Analysis of Coordination Environments in Oxides. *Chem. Mater.* **2017**, *29*, 8346−8360.

(28) Bartók, A. P.; Kondor, R.; Csányi, G. On Representing Chemical Environments. *Phys. Rev. B* **2013**, *87*, 184115.

(29) Rupp, M.; Tkatchenko, A.; Müller, K.-R.; von Lilienfeld, O. A. Fast and Accurate Modeling of Molecular Atomization Energies with Machine Learning. *Phys. Rev. Lett.* **2012**, *108*, No. 058301.

(30) Huo, H.; Rupp, M. Unified Representation of Molecules and Crystals for Machine Learning. *arXiv*, 2018, 1704.06439; https://arxiv.org/abs/1704.06439 (accessed December 14, 2021).

(31) Cumby, J.; Attfield, J. P. Ellipsoidal Analysis of Coordination Polyhedra. *Nat. Commun.* **2017**, *8*, 14235.
(32) Perez-Mato, J. M.; Orobengoa, D.; Aroyo, M. I. Mode Crystallography of Distorted Structures. *Acta Crystallogr., Sect. A: Found. Adv.* **2010**, *66*, 558−590.
(33) Kerman, S.; Campbell, B. J.; Satyavarapu, K. K.; Stokes, H. T.; Perselli, F.; Evans, J. S. O. The superstructure determination of displacive distortionsviasymmetry-mode analysis. *Acta Crystallogr., Sect. A: Found. Crystallogr.* **2012**, *68*, 222−234.
(34) Islam, M. A.; Rondinelli, J. M.; Spanier, J. E. Normal Mode Determination of Perovskite Crystal Structures with Octahedral Rotations: Theory and Applications. *J. Phys.: Condens. Matter* **2013**, *25*, 175902.
(35) Schranz, W.; Rychetsky, I.; Hlinka, J. Polarity of Domain Boundaries in Nonpolar Materials Derived from Order Parameter and Layer Group Symmetry. *Phys. Rev. B* **2019**, *100*, 184105.
(36) Mochizuki, Y.; Sung, H.-J.; Takahashi, A.; Kumagai, Y.; Oba, F. Theoretical Exploration of Mixed-Anion Antiperovskite Semiconductors M_3XN(M = Mg,Ca,Sr,Ba; X = P,As,Sb,Bi). *Phys. Rev. Mater.* **2020**, *4*, No. 044601.
(37) Yang, R. X.; Skelton, J. M.; da Silva, E. L.; Frost, J. M.; Walsh, A. Assessment of Dynamic Structural Instabilities Across 24 Cubic Inorganic Halide Perovskites. *J. Chem. Phys.* **2020**, *152*, No. 024703.
(38) Howard, C. J.; Stokes, H. T. Group-Theoretical Analysis of Octahedral Tilting in Perovskites. *Acta Crystallogr., Sect. B: Struct. Sci.* **1998**, *54*, 782−789.
(39) Wagner, N.; Puggioni, D.; Rondinelli, J. M. Learning from Correlations Based on Local Structure: Rare-Earth Nickelates Revisited. *J. Chem. Inf. Model.* **2018**, *58*, 2491−2501.
(40) Lewis, J. W.; Payne, J. L.; Evans, I. R.; Stokes, H. T.; Campbell, B. J.; Evans, J. S. O. An Exhaustive Symmetry Approach to Structure Determination: Phase Transitions in $Bi_2Sn_2O_7$. *J. Am. Chem. Soc.* **2016**, *138*, 8031−8042.
(41) Castelli, I. E.; Olsen, T.; Datta, S.; Landis, D. D.; Dahl, S.; Thygesen, K. S.; Jacobsen, K. W. Computational Screening of Perovskite Metal Oxides for Optimal Solar Light Capture. *Energy Environ. Sci.* **2012**, *5*, 5814−5819.
(42) Fabini, D. H.; Laurita, G.; Bechtel, J. S.; Stoumpos, C. C.; Evans, H. A.; Kontos, A. G.; Raptis, Y. S.; Falaras, P.; Van der Ven, A.; Kanatzidis, M. G.; et al. Dynamic Stereochemical Activity of the Sn^{2+} Lone Pair in Perovskite $CsSnBr_3$. *J. Am. Chem. Soc.* **2016**, *138*, 11820−11832.
(43) Correa-Baena, J.-P.; Nienhaus, L.; Kurchin, R. C.; Shin, S. S.; Wieghold, S.; Putri Hartono, N. T.; Layurova, M.; Klein, N. D.; Poindexter, J. R.; Polizzotti, A.; Sun, S.; Bawendi, M. G.; Buonassisi, T. A-Site Cation in Inorganic $A_3Sb_2I_9$ Perovskite Influences Structural Dimensionality, Exciton Binding Energy, and Solar Cell Performance. *Chem. Mater.* **2018**, *30*, 3734−3742.
(44) Filip, M. R.; Giustino, F. The Geometric Blueprint of Perovskites. *Proc. Natl. Acad. Sci. U. S. A.* **2018**, *115*, 5397−5402.
(45) Maughan, A. E.; Ganose, A. M.; Scanlon, D. O.; Neilson, J. R. Perspectives and Design Principles of Vacancy-Ordered Double Perovskite Halide Semiconductors. *Chem. Mater.* **2019**, *31*, 1184−1195.
(46) Tao, Q.; Xu, P.; Li, M.; Lu, W. Machine Learning for Perovskite Materials Design and Discovery. *npj Comput. Mater.* **2021**, *7*, 23.
(47) Talapatra, A.; Uberuaga, B. P.; Stanek, C. R.; Pilania, G. A Machine Learning Approach for the Prediction of Formability and Thermodynamic Stability of Single and Double Perovskite Oxides. *Chem. Mater.* **2021**, *33*, 845−858.
(48) Tinkham, M. *Group Theory and Quantum Mechanics*; Dover Publications, Inc.: 2003.
(49) Togo, A.; Tanaka, I. First Principles Phonon Calculations in Materials Science. *Scr. Mater.* **2015**, *108*, 1−5.
(50) Dresselhaus, M. S.; Dresselhaus, G.; Jorio, A. *Group Theory: Application to the Physics of Condensed Matter*; Springer Science & Business Media: 2007.
(51) Kuhn, H. W. The Hungarian Method for the Assignment Problem. *Naval research logistics quarterly* **1955**, *2*, 83−97.
(52) Ong, S. P.; Richards, W. D.; Jain, A.; Hautier, G.; Kocher, M.; Cholia, S.; Gunter, D.; Chevrier, V. L.; Persson, K. A.; Ceder, G. Python Materials Genomics (Pymatgen): A Robust, Open-Source Python Library for Materials Analysis. *Comput. Mater. Sci.* **2013**, *68*, 314−319.
(53) Goodall, R. E. A.; Lee, A. A. Order Matters: Sequence to Sequence for Sets. *arXiv*, 2016, 1511.06391; https://arxiv.org/abs/1511.06391 (accessed December 14, 2021).
(54) Pedregosa, F.; et al. Scikit-learn: Machine Learning in Python. *J. Mach. Learn Res.* **2011**, *12*, 2825−2830.
(55) Jain, A.; Ong, S. P.; Hautier, G.; Chen, W.; Richards, W. D.; Dacek, S.; Cholia, S.; Gunter, D.; Skinner, D.; Ceder, G.; Persson, K. A. Commentary: The Materials Project: A Materials Genome Approach to Accelerating Materials Innovation. *APL Mater.* **2013**, *1*, No. 011002.
(56) Ong, S. P.; Cholia, S.; Jain, A.; Brafman, M.; Gunter, D.; Ceder, G.; Persson, K. A. The Materials Application Programming Interface (API): A Simple, Flexible and Efficient API for Materials Data Based On Representational State Transfer (Rest) Principles. *Comput. Mater. Sci.* **2015**, *97*, 209−215.
(57) Togo, A.; Tanaka, I. Spglib: A Software Library for Crystal Symmetry Search. *arXiv*, 2018, 1808.01590; https://arxiv.org/abs/1808.01590 (accessed December 14, 2021).
(58) Blöchl, P. E. Projector Augmented-Wave Method. *Phys. Rev. B* **1994**, *50*, 17953.
(59) Kresse, G.; Furthmüller, J. Efficiency of Ab-Initio Total Energy Calculations for Metals and Semiconductors Using a Plane-Wave Basis Set. *Comput. Mater. Sci.* **1996**, *6*, 15−50.
(60) Kresse, G.; Furthmüller, J. Efficient Iterative Schemes for Ab Initio Total-Energy Calculations Using a Plane-Wave Basis Set. *Phys. Rev. B* **1996**, *54*, 11169.
(61) *VISE*, v0.1.13; GitHub repository. https://github.com/kumagai-group/vise (accessed December 14, 2021).
(62) Perdew, J. P.; Burke, K.; Ernzerhof, M. Generalized gradient approximation made simple. *Phys. Rev. Lett.* **1996**, *77*, 3865.
(63) Heyd, J.; Scuseria, G. E.; Ernzerhof, M. Hybrid Functionals Based on a Screened Coulomb Potential. *J. Chem. Phys.* **2003**, *118*, 8207−8215.
(64) Momma, K.; Izumi, F. Vesta 3 for Three-Dimensional Visualization of Crystal, Volumetric and Morphology Data. *J. Appl. Crystallogr.* **2011**, *44*, 1272−1276.
(65) Frost, J. M.; Butler, K. T.; Walsh, A. Molecular ferroelectric contributions to anomalous hysteresis in hybrid perovskite solar cells. *APL Mater.* **2014**, *2*, No. 081506.
(66) Mattoni, A.; Filippetti, A.; Caddeo, C. Modeling hybrid perovskites by molecular dynamics. *J. Phys.: Condens. Matter* **2017**, *29*, No. 043001.
(67) Csonka, G. I.; Perdew, J. P.; Ruzsinszky, A.; Philipsen, P. H. T.; Lebègue, S.; Paier, J.; Vydrov, O. A.; Ángyán, J. G. Assessing the performance of recent density functionals for bulk solids. *Phys. Rev. B* **2009**, *79*, 155107.
(68) Indenbom, V. Phase Transitions Without Change of the Atom Number in the Crystal Unit Cell. *Kristallografiya* **1960**, *5*, 115−125.
(69) Levanyuk, A. P.; Sannikov, D. G. Improper Ferroelectrics. *Phys.-Usp.* **1974**, *17*, 199−214.
(70) Benedek, N. A.; Fennie, C. J. Why Are There So Few Perovskite Ferroelectrics? *J. Phys. Chem. C* **2013**, *117*, 13339−13349.
(71) Wang, J.; Neaton, J. B.; Zheng, H.; Nagarajan, V.; Ogale, S. B.; Liu, B.; Viehland, D.; Vaithyanathan, V.; Schlom, D. G.; Waghmare, U. V.; Spaldin, N. A.; Rabe, K.; Wuttig, M.; Ramesh, R. Epitaxial $BiFeO_3$ Multiferroic Thin Film Heterostructures. *Science* **2003**, *299*, 1719−1722.
(72) Neaton, J. B.; Ederer, C.; Waghmare, U. V.; Spaldin, N. A.; Rabe, K. First-principles study of spontaneous polarization in multiferroic $BiFeO_3$. *Phys. Rev. B* **2005**, *71*, No. 014113.
(73) Walsh, A.; Payne, D. J.; Egdell, R. G.; Watson, G. W. Stereochemistry of Post-Transition Metal Oxides: Revision of the Classical Lone Pair Model. *Chem. Soc. Rev.* **2011**, *40*, 4455−4463.

(74) Van der Maaten, L.; Hinton, G. Visualizing data using t-SNE. *J. Mach. Learn Res.* **2008**, *9*, 2579−2605.
(75) Pedregosa, F.; et al. Scikit-Learn: Machine Learning in PYthon. *J. Mach. Learn Res.* **2011**, *12*, 2825−2830.
(76) Iasir, A. R. M.; Lombardi, T.; Lu, Q.; Mofrad, A. M.; Vaninger, M.; Zhang, X.; Singh, D. J. Electronic and magnetic properties of perovskite selenite and tellurite compounds: $CoSeO_3$, $NiSeO_3$, $CoTeO_3$, and $NiTeO_3$. *Phys. Rev. B* **2020**, *101*, No. 045107.
(77) Sawaguchi, E.; Akishige, Y.; Yamamoto, T.; Nakahara, J. Phase Transition in Hexagonal Type $BaTiO_3$. *Ferroelectrics* **1989**, *95*, 29−36.
(78) Hashemizadeh, S.; Biancoli, A.; Damjanovic, D. Symmetry Breaking in Hexagonal and Cubic Polymorphs of $BaTiO_3$. *J. Appl. Phys.* **2016**, *119*, No. 094105.
(79) Ogawa, N.; Ogimoto, Y.; Ida, Y.; Nomura, Y.; Arita, R.; Miyano, K. Polar Antiferromagnets Produced with Orbital Order. *Phys. Rev. Lett.* **2012**, *108*, 157603.
(80) Gupta, K.; Mahadevan, P.; Mavropoulos, P.; Ležaić, M. Orbital-Ordering-Induced Ferroelectricity in $SrCrO_3$. *Phys. Rev. Lett.* **2013**, *111*, No. 077601.
(81) Ding, Y.; Cao, L.; Wang, W.; Jing, B.; Shen, X.; Yao, Y.; Xu, L.; Li, J.; Jin, C.; Yu, R. Bond Length Fluctuation in Perovskite Chromate $SrCrO_3$. *J. Appl. Phys.* **2020**, *127*, No. 075106.
(82) Parsaeifard, B.; Sankar De, D.; Christensen, A. S; Faber, F. A; Kocer, E.; De, S.; Behler, J.; Anatole von Lilienfeld, O.; Goedecker, S. An assessment of the structural resolution of various fingerprints commonly used in machine learning. *Mach. Learn.: Sci. Technol.* **2021**, *2*, No. 015018.
(83) Fung, V.; Zhang, J.; Juarez, E.; Sumpter, B. G. Benchmarking graph neural networks for materials chemistry. *npj Comp. Mater.* **2021**, *7*, 84.

https://doi.org/10.1021/acs.chemmater.1c02959
Chem. Mater. 2022, 34, 562−573